Climatology of Tibetan Plateau Vortices in reanalysis data and a high-resolution global climate model

It is advisable to refer to the publisher's version if you intend to cite from the work. See Guidance on citing.

www.reading.ac.uk/centaur

Climatology of Tibetan Plateau Vortices in Reanalysis Data and a High-Resolution Global Climate Model

JULIA CURIO, REINHARD SCHIEMANN, KEVIN I. HODGES, AND ANDREW G. TURNER

National Centre for Atmospheric Science, and Department of Meteorology, University of Reading, Reading, United Kingdom

ABSTRACT

The Tibetan Plateau (TP) and surrounding high mountains constitute an important forcing of the atmospheric circulation due to their height and extent, and thereby impact weather and climate in downstream regions of East Asia. Mesoscale Tibetan Plateau vortices (TPVs) are one of the major precipitation-producing systems on the TP. A fraction of TPVs move off the TP to the east and can trigger extreme precipitation in parts of China, such as the Sichuan province and the Yangtze River valley, which can result in severe flooding. In this study, the climatology of TPV occurrence is examined in two reanalyses and, for the first time, in a high-resolution global climate model using an objective feature tracking algorithm. Most TPVs are generated in the northwestern part of the TP; the center of this main genesis region is small and stable throughout the year. The strength and position of the subtropical westerly jet is correlated to the distance TPVs can travel eastward and therefore could have an effect on whether or not a TPV is moving off the TP. TPV-associated precipitation can account for up to 40% of the total precipitation in parts of China in selected months, often due to individual TPVs. The results show that the global climate model is able to simulate TPVs at N512 (~25 km) horizontal resolution and in general agrees with the reanalyses. The fact that the global climate model can represent the TPV climatology opens a wide range of options for future model-based research on TPVs.

1. Introduction

The Tibetan Plateau (TP) is the highest and largest plateau in the world and often called "the world water tower" (Xu et al. 2008). The TP is the origin of many large Asian rivers, including the Ganges, Brahmaputhra, Indus, Yangtze, Yellow River, and Mekong, which provide water for billions of people downstream. The Asian monsoon and midlatitude westerlies are the main atmospheric circulation features influencing weather and climate of the TP. Due to its average height of more than 4500 m and its large extent, the TP in turn shapes the large-scale atmospheric circulation, through dynamic and thermal effects, and therefore the weather and climate of large parts of Asia (both surrounding and downstream regions).

Tibetan Plateau vortices (TPVs) are known to be one of the major precipitation-producing systems on the Tibetan Plateau (Wang 1987). They are present at the 500-hPa level, with a vertical extent of 2–3 km and a horizontal scale of 400–800 km (Lin 2015), making them mesoscale features. TPVs originate on the TP and the majority of TPVs remain on the TP throughout their lifetime, while a smaller number move off the plateau to the east. These "moving-off" TPVs can trigger extreme precipitation and severe flooding over large parts of eastern and southern China (e.g., in Sichuan province and the Yangtze valley) (Tao and Ding 1981; Feng et al. 2014). Feng et al. (2014) describe a TPV event that lasted from 19 to 24 July 2008 in which a TPV moved off the TP and traveled northeastward all the way to the coast of the Yellow Sea within five days. They report that this TPV caused heavy precipitation along its path, especially in Sichuan province, where the maximum 24-h accumulated precipitation at one station reached 288.4 mm (roughly a quarter of the average annual precipitation at that location).

The climatology of TPVs has so far been examined using objective tracking approaches applied to reanalysis datasets, such as ERA-Interim (Lin 2015) and NCEP-CFSR (Feng et al. 2014). Feng et al. (2014) identified TPVs in the 500-hPa streamline and relative vorticity fields of the NCEP-CFSR reanalysis for 10 summer seasons (April–October, 2000–09). Their results for the geographical distribution of TPV genesis show that the region within 31°–36°N, 84°–94°E produces two-thirds of all TPVs, and that 33°–36°N, 84°–90°E is the most active region. Lin (2015) identified and tracked TPVs using the 500-hPa geopotential height field of ERA-Interim. Their method results in a dataset of TPV activity, which shows on average 60 TPVs per year, with a moving-off rate of around 10%. They find the highest number of TPVs in summer and show that the most intense TPVs occur in the rainy season from May to September.

Previous studies using model simulations and sensitivity experiments have been performed for case studies to examine the development and maintenance of specific observed TPVs (Dell'Osso and Chen 1986; Wang 1987; Zhu et al. 2003; Zhao 2015). These studies have focused on events causing extreme precipitation downstream of the TP. So far no studies have been conducted using model simulations for longer periods, in order to test the ability of models to simulate the long-term statistics of seasonality, genesis, and propagation of TPVs. Therefore one open question is how well global climate models can represent the TPV climatology. The answer to this question will have implications for future numerical experiments investigating the mechanisms leading to TPV generation and the predictive skill of TPV activity.

The primary aim of this study is to assess how well a high-resolution global climate model represents the climatology of TPVs, including their spatial distribution and annual cycle. To answer this question we first identify and track TPVs in two reanalysis datasets, ERA-Interim and NCEP-CFSR. We also do the same in a set of present-climate, high-resolution, atmosphere-only global climate model simulations performed in the UPSCALE project [UK on PRACE (Partnership for Advanced Computing in Europe): Weather-Resolving Simulations of Climate for Global Environmental Risk; Mizielinski et al. 2014]. The obtained model TPV climatology is then compared to the reanalysis climatologies for all tracked TPVs and for different selected subsamples (e.g., moving-off TPVs).

Secondary aims of this study are to connect TPV occurrence and behavior to the large-scale circulation, in particular the subtropical westerly jet, and to analyze the importance of TPV-associated precipitation downstream of the TP.

The manuscript is organized as follows. Section 2 describes the data used and introduces the methodology for identifying and tracking the TPVs. The results of the tracking for the different datasets are described, compared, and discussed in sections 3–7. To assess how well the GA3 simulations (defined in section 2b) represent the TPV climatology we examine the model performance using different metrics. First we establish the climatology in the reanalyses and then compare with results from the model. We start with the description of the annual cycle of TPV occurrence in all three datasets and for three different groups of TPVs in section 3. In a second step we examine the spatial statistics for different groups of TPVs and the connection to the large-scale circulation in section 4. We analyze and compare the lifetime and the distance TPVs travel in section 5 and examine the precipitation associated with TPVs in section 6. In section 7 we discuss the interannual variability of TPV occurrence. Finally, we summarize the results and draw conclusions with respect to the aims of the study in section 8.

2. Data and methodology

ERA-Interim (Dee et al. 2011) and NCEP-CFSR (Saha et al. 2010) reanalysis data, and the UPSCALE (Mizielinski et al. 2014) simulations at 6-hourly temporal resolution are used to identify and track TPVs.

a. Reanalysis data

ERA-Interim spans the period 1979–2015 and has a spatial resolution of ~80 km (T255) on 60 vertical levels. For this study, the NCEP-CFSR reanalysis dataset, covering 1979–2010, has been expanded to 2015 using the operational analysis NCEP-CFS version 2 (Saha et al. 2014) for the years 2011–15. NCEP-CFSR has a spatial resolution of ~38 km (T382) on 64 vertical levels. Both reanalysis datasets have been successfully employed before to obtain TPV climatologies, using different identification and tracking approaches (e.g., Feng et al. 2014; Lin 2015), and are therefore suitable for the use in the current study.

b. Model data

Since we hypothesize that the interaction of the jet stream with steep orography may be implicated in the genesis of TPVs, we choose a high-resolution GCM for this study. The effects of resolution on the simulation and structure of TPVs will be reported in a future publication. For the UPSCALE project an ensemble of HadGEM3 (Hadley Centre Global Environment Model 3) Global Atmosphere 3.0 (GA3; Walters et al. 2011) present-climate atmosphere-only simulations

were performed for different horizontal resolutions [N512 (~25 km), N216 (~60 km), and N96 (~130 km)]. Here we use the simulations with the highest horizontal resolution of ~25 km (N512). Apart from the daily sea surface temperature (SST) and sea ice forcings, derived from the Operational Sea Surface Temperature and Sea Ice Analysis (OSTIA) product (Donlon et al. 2012), the ensemble is configured mainly following the Atmospheric Model Intercomparison Project II (AMIP-II) standard. Each of the five ensemble members was perturbed by randomly changing the lowest-order bit in the potential temperature field of the initial conditions (Mizielinski et al. 2014). The GA3 simulations cover the period 1985–2011, providing data for 27 years. Here we only use the complete years 1986–2011. The results from the free-running global climate model can only be compared with the reanalysis results from a climatological point of view and not for specific TPV cases.

c. TRACK

In this study, TPVs are identified and tracked using an objective feature-tracking algorithm (TRACK) developed by Hodges (1994, 1995, 1999). TRACK has previously been used in the analysis of extratropical cyclones (Hodges et al. 2011; Hoskins and Hodges 2002; Zappa et al. 2013), tropical cyclones (Bengtsson et al. 2007), Mediterranean hurricanes or Medicanes (Tous et al. 2016), and polar lows (Zappa et al. 2014). The TRACK settings used in this study are similar to the ones used for polar lows (Zappa et al. 2014) due to the similar horizontal scale of polar lows and TPVs. The tracking parameters have also been adjusted to account for the reduced sampling frequency (6-hourly compared to 3-hourly for polar lows).

TPVs are identified and tracked as maxima in the 6-hourly 500-hPa spatially spectrally filtered relative vorticity field. The spectral filtering removes total wavenumbers smaller than 40 (large spatial scale, >1000 km) and larger than 100 (small spatial scale, <400 km), hence focusing on the TPV spatial scale. The spectral coefficients are also tapered using the method of Sardeshmukh and Hoskins (1984) to further reduce noise in the data such as Gibbs oscillations. During the spectral filtering the data for all three datasets are output onto the same T255 Gaussian grid (512 × 256) as used for ERA-Interim. The cyclones are identified as the off-grid maxima greater than $2 \times 10^{-5}\,\text{s}^{-1}$ using B-spline interpolation and a steepest-ascent method (Hodges 1995).

The tracking proceeds by first initializing tracks by connecting the maxima using a nearest-neighbor method. These tracks are then refined by minimizing a cost function for track smoothness subject to adaptive constraints on the track smoothness and displacement distance in a time step (Hodges 1999). At this stage all vorticity maxima are tracked before other criteria are applied to identify the TPVs, as this approach maximizes the proportion of the TPV life cycle identified.

Cyclones are retained that originate on the TP, using the 3000-m altitude line as the TP's perimeter, and that persist for at least four time steps (one day). The altitude threshold serves to exclude western disturbances (Dimri et al. 2015), which also occur at the 500-hPa level and travel eastward along the southern slopes of the Himalayas embedded in the subtropical westerly jet (SWJ). In a second step we apply a geopotential minimum filter, which means that at least for one time step per TPV track an associated 500-hPa geopotential height minimum has to occur within a search radius of 2.5° (geodesic radius) around the track point. Figure 1 shows an example of the outputted tracks for July 2008 for ERA-Interim.

Moving-off TPVs are defined as those TPVs that travel farther east than 105°E, roughly coincident with the eastern boundary of the TP as defined by the 3000-m contour.

As is common in other tracking studies, spatial statistics (i.e., genesis, lysis, and track densities) are computed from the TPV tracks for each dataset using the spherical kernel approach (Hodges 1996). The genesis (lysis) is defined as the first (last) time step a TPV is identified, while the track refers to all time steps of an identified TPV. The densities for genesis, track, and lysis are compared between the two reanalysis data and the GA3 simulations.

In a companion study (Curio et al. 2018) results from the TPV database derived from ERA-Interim using TRACK were compared to TPVs manually identified using radiosonde data (data from yearbooks of TPVs published by the Institute of Plateau Meteorology, Chengdu). The comparison for 20 cases showed that the two methods agree for cases where the underlying data (ERA-Interim and observations from sounding stations) are in good agreement. This demonstrates the suitability of using TRACK to study TPVs.

d. TPV-associated precipitation

In a further step, the area-averaged precipitation amount within a search area of 3° geodesic radius around each tracked point of a TPV is associated with that tracked point. This search area is larger than for the geopotential height minima (2.5° geodesic radius) because precipitation produced by the TPVs stretches farther away from the TPV center whereas the geopotential minimum should be close to the vorticity center.
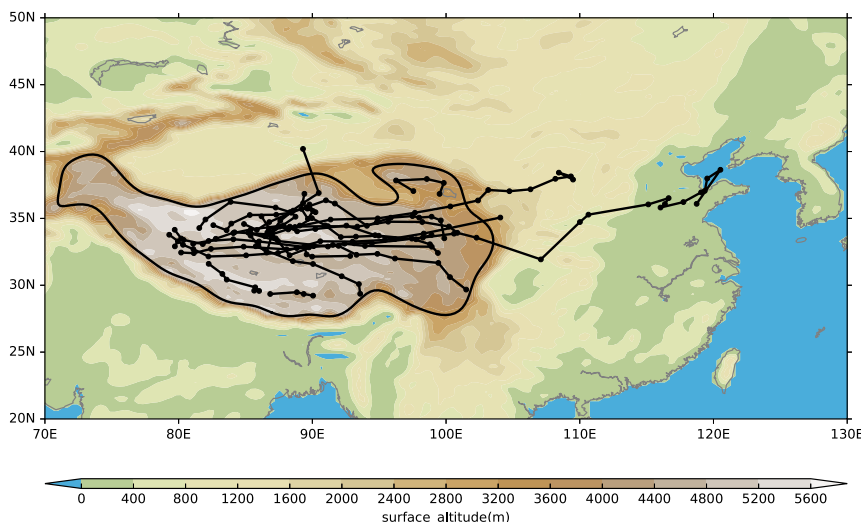
FIG. 1. Example TPV tracks (black lines) of July 2008 in ERA-Interim at each time step during the track (black dots). The boundary of the TP is indicated using the 3000-m contour.

For ERA-Interim, the 6-h accumulation precipitation forecast field with a lead time of 12 h is used to avoid errors arising during spinup. For NCEP-CFSR we use the 6-h average precipitation rate from the flux files (forecast for the first 6 h). The GA3 precipitation was resampled from the original 3-hourly resolution to 6-hourly resolution to match the temporal resolution of the tracking results. ERA-Interim is known to reproduce well the climatology and interannual variability of precipitation, such as global monsoon precipitation (Lin et al. 2014) and East Asian summer monsoon precipitation (Huang et al. 2016), which might be due to the advanced 12-h 4DVAR data assimilation method (Lin et al. 2014).

We calculate the value corresponding to the 95th percentile of the maximum attained precipitation along TPV tracks for ERA-Interim (1.11 mm h^{-1}), NCEP-CFSR (0.71 mm h^{-1}), and the five GA3 ensemble members (0.74, 0.78, 0.79, 0.74, and 0.76 mm h^{-1}). The 95th percentile threshold is used in order to subsample TPVs that exhibit an associated precipitation amount above this threshold at least once during their lifetime. Here, TPVs that meet this condition are termed heavy-rain TPVs.

To examine the importance of TPVs for the precipitation over the TP and the downstream regions, spatial masks of the area within a geodesic radius of 3° around all track points at each time step are used to mask the precipitation field; this allows us to retain only the precipitation within these regions and subsequently generate maps of TPV-associated precipitation. We can then calculate the ratio between TPV-associated precipitation and the total precipitation for each month and for the climatological average.

3. Annual cycle of TPV occurrence

In total 5697 TPVs (~154 per year) were identified and tracked in ERA-Interim, of which 1155 TPVs move farther east than 105°E and are therefore classified as moving-off TPVs (~31 per year) (see Table 1). For NCEP-CFSR both numbers are higher, 9949 TPVs in total (~269 per year), and 1957 moving-off TPVs (~53 per year). The moving-off cases account for ~20% of all TPVs in ERA-Interim and NCEP-CFSR.

The GA3 simulations produce on average 6310 TPVs (~242 per year), and 1663 moving-off TPVs (~64 per year), resulting in a slightly higher moving-off ratio (~26%) than for the reanalysis datasets.

We start to establish a TPV climatology by first examining the annual cycle of TPV occurrence (number of generated TPVs) for the different datasets (ERA-Interim, NCEP-CFSR, GA3) as well as the three different subsamples (all, moving-off, heavy-rain TPVs).

Figure 2 shows the annual cycle of all TPVs, as well as the moving-off cases and heavy-rain TPVs (see section 2d). In ERA-Interim the highest number of TPVs occurs in the extended summer season (April to September), whereas the lowest number occurs in winter (November–February), making a clear annual cycle.

TABLE 1. Number of TPVs identified in each of the three datasets in total and for the two subsamples: moving-off and heavy-rain TPVs.

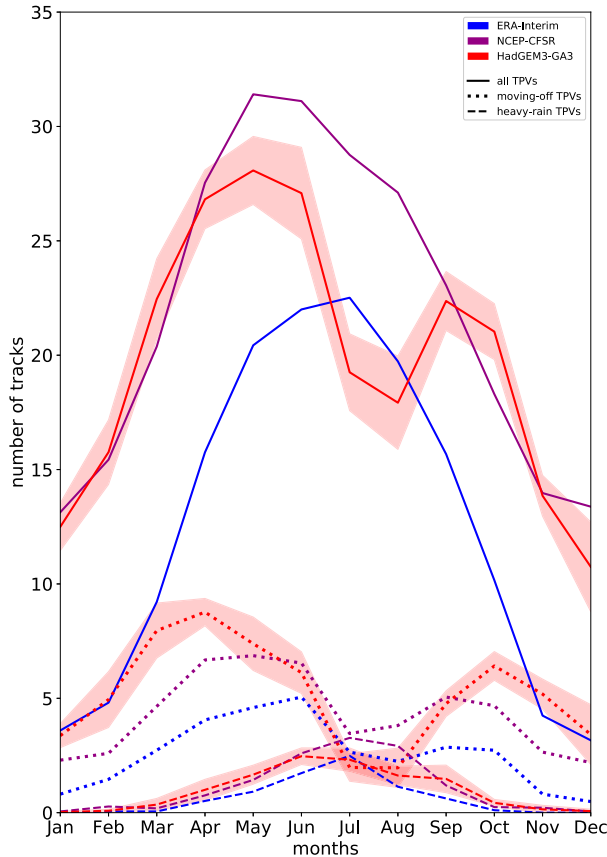| No. of TPVs	ERA-Interim	NCEP-CFSR	GA3
Total	154	269	242
Moving-off	31 (20%)	53 (20%)	64 (26%)
Heavy-rain	7.7 (5%)	13.5 (5%)	12.1 (5%)

FIG. 2. Number of all identified TPVs, the moving-off cases, and the top 5% of precipitating TPVs per month, averaged over all available years, respectively for ERA-Interim (blue), NCEP-CFSR (purple), and the HadGEM3-GA3 ensemble mean (red). The red shading covers the spread between the five GA3 ensemble members, its upper and lower boundary is defined as $\pm 2\sigma$ from the mean over the five ensemble members, respectively.

The annual cycles for ERA-Interim and NCEP-CFSR are very similar, the only difference being the number of TPVs, with ERA-Interim having on average around 10 fewer TPVs per month than NCEP-CFSR, and a shift of the maximum from July for ERA-Interim toward May for NCEP-CFSR. Similar distributions are found by Lin (2015) and Feng et al. (2014) using independent identification and tracking methods. The number of TPVs found in each month by Feng et al. (2014) is very close to our results, while Lin (2015) identified around 50% fewer TPVs in ERA-Interim (1979–2013). The use of a different tracking algorithm and a different variable (500-hPa geopotential height) are possible reasons for the different number of TPVs identified by Lin (2015).

The GA3 ensemble mean shows a different (bimodal) annual cycle, with maxima in spring and autumn and minima in summer and winter. In GA3 the

peak in TPVs occurs in May, two months earlier than in ERA-Interim but at the same time as in NCEP-CFSR. In winter, spring, and autumn the number of TPVs is very close to the number of TPVs found in NCEP-CFSR. In general the spread of the UPSCALE ensemble members is relatively small, showing that differences between the three datasets are not simply due to internal variability.

For the subsample of moving-off TPVs the two reanalysis datasets show very similar annual cycles, with only a small offset of less than two tracks per month. The number of moving-off TPVs is highest in spring and autumn and lowest in winter and summer. However, the annual cycle for the GA3 ensemble is more pronounced compared to the reanalysis data.

Lin (2015) also find the highest number of moving-off TPVs in spring, but it is difficult to compare the results since they allow TPVs to move off the TP in any direction, whereas in this study TPVs have to move east of 105°E to be considered as moving-off TPVs.

The higher number of moving-off TPVs in spring and autumn may be caused by the position and strength of the SWJ at these times, which is located over the Tibetan Plateau during the transition from its winter position (south of the TP) to the summer location (north of the TP) (Schiemann et al. 2009). The connection of TPV occurrence to the SWJ is discussed further in section 4a.

Heavy-rain TPVs occur predominantly in summer, when there are about two such TPVs per month. In winter, TPVs associated with heavy precipitation do not occur at all, due to the dry conditions over the Tibetan Plateau and the generally negligible amounts of precipitation (Maussion et al. 2014; Bookhagen and Burbank 2010), except for the westernmost high mountain parts of the TP. For the heavy-rain TPVs all datasets show almost the same annual cycle and similar numbers of TPVs. Our motivation to study heavy-rain TPVs derives from the potentially hazardous nature of individual systems, irrespective of the contribution of these events to total precipitation.

4. Spatial statistics

In the following sections we will show the spatial statistics for three different metrics (genesis, track, and lysis density) for each of the three subsamples separately. We start with a detailed description for the group of all TPVs, including the connection to the SWJ, before discussing the moving-off and heavy-rain TPVs.

a. All TPVs

Since TPVs mainly occur during the extended summer season (April–September), the analysis focuses on three
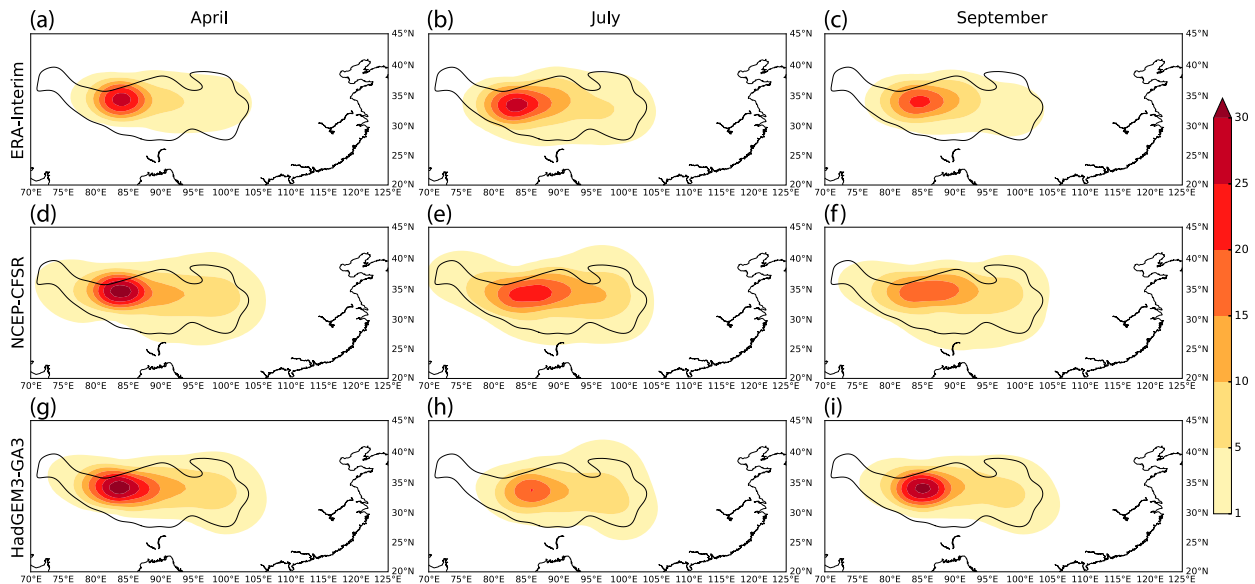
FIG. 3. Genesis density of all TPVs for (a)–(c) ERA-Interim, (d)–(f) NCEP-CFSR, and (g)–(i) the HadGEM3-GA3 ensemble mean for (left) April, (center) July, and (right) September. The color shading shows the genesis density in number per month per unit area (using a 5° spherical cap). The boundary of the TP is indicated using the 3000-m contour.

months, April, July, and September, which covers most key features of the annual cycle.

GENESIS

In this section, we analyze where TPVs are generated on the TP and compare the location and strength of the genesis region in different months and for all three datasets.

Figure 3 shows the genesis densities of the TPVs for the three datasets for the three selected months (April, July, September), covering the active period and most of the key features of the seasonal cycle (see Fig. 2). For the GA3 simulations the ensemble mean is shown. While TPVs can form anywhere on the TP, the main genesis region in ERA-Interim (Figs. 3a–c) is located in the northwestern part of the central TP, and is relatively small and stable throughout the year. The highest genesis densities occur in the region between 33° to 34°N and 83° to 85°E in spring and summer, and are slightly lower and slightly shifted eastward in autumn. The higher number of TPVs generated in summer compared to other seasons in ERA-Interim (Fig. 2) does not result in higher maximum genesis densities in summer, since the main genesis region is larger, so the higher number of TPVs is generated in a larger area.

In general, NCEP-CFSR and ERA-Interim agree on the strength and spatial distribution of the genesis densities. Compared to ERA-Interim, TPVs are generated over a larger area on the TP in NCEP-CFSR (Figs. 3d–f) and the area of higher genesis densities spreads farther east from the main genesis region, resulting in slightly higher genesis densities in the eastern part of the TP. In July and September the local maximum in the main genesis region is not as pronounced as in ERA-Interim. NCEP-CFSR generates TPVs also in the westernmost part of the TP, where no TPVs are generated in ERA-Interim.

The reanalysis data and the GA3 simulations show similar results; the spatial patterns and magnitudes are generally in close agreement. In April the GA3 (Fig. 3g) ensemble shows slightly higher genesis densities than ERA-Interim in the main genesis region and in the eastern part of the TP. Compared to NCEP-CFSR the GA3 ensemble mean shows nearly the same values for the genesis density and its spatial distribution. In July, GA3 (Fig. 3h) exhibits lower maximum densities compared to ERA-Interim, which matches the generally lower number of identified TPVs in summer in the GA3 ensemble compared to ERA-Interim and NCEP-CFSR as shown in the annual cycle of TPV occurrence (Fig. 2). This difference in July could be caused by differences in the atmospheric circulation (e.g., the strength of the Tibetan high and the magnitude of the northward shift of the SWJ). In September the GA3 ensemble exhibits higher maximum genesis densities than the two reanalysis datasets. The west–east and north–south extensions of the genesis region in the GA3 ensemble are between those of ERA-Interim and NCEP-CFSR.

These results for the TPV genesis are in agreement with previous studies highlighting the region between
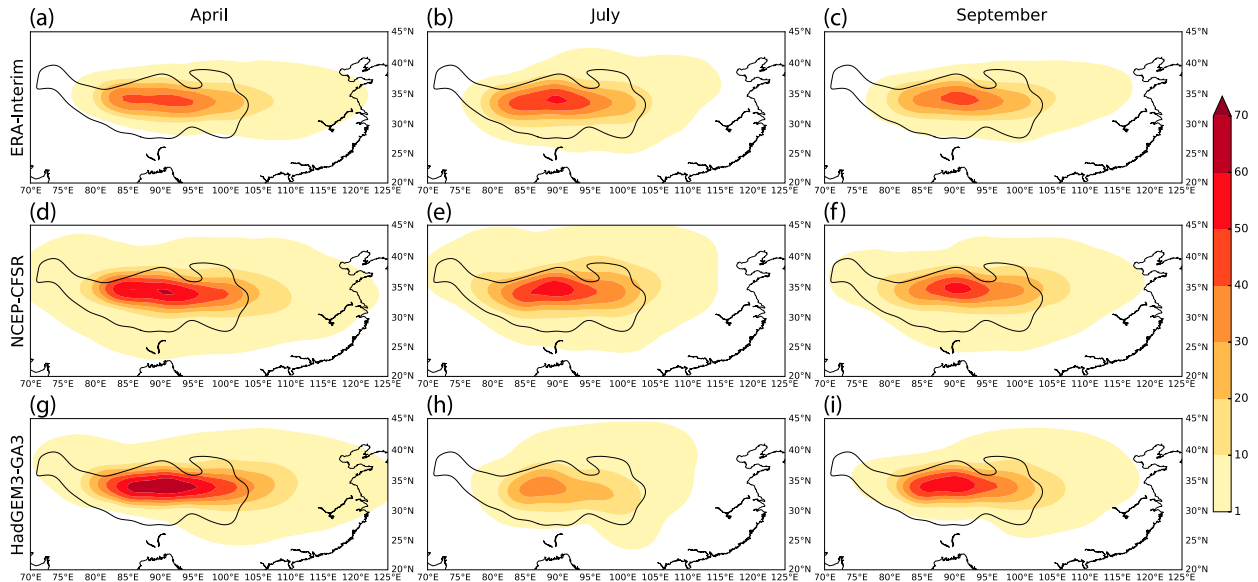
FIG. 4. Track density of all TPVs for (a)–(c) ERA-Interim, (d)–(f) NCEP-CFSR, and (g)–(i) the HadGEM3-GA3 ensemble mean for (left) April, (center) July, and (right) September. The color shading shows the track density in number per month per unit area (using a 5° spherical cap). The boundary of the TP is indicated using the 3000-m contour.

33° and 36°N and 84° and 90°E (Feng et al. 2014) as the main region of TPV genesis. Lin (2015) identify the main genesis region only a few degrees farther east. As discussed above, direct quantitative comparisons between these datasets are difficult.

(i) Track

The spatial distribution of TPV tracks, the track density, for both reanalyses and the GA3 ensemble mean is shown in Fig. 4.

Figure 4 shows that TPVs mainly move eastward from their genesis region in a band of high track densities along 34°N. In April and September the main track path is elongated along a west–east axis and reaches into central China, while it only covers a few degrees of latitude.

The two reanalysis datasets show very similar results regarding the spatial distribution of TPV occurrence, with NCEP showing slightly higher densities over the TP for all three months, especially in April.

In April (Figs. 4a,d,g) the track densities in GA3 are only slightly higher compared to NCEP-CFSR but substantially higher compared to ERA-Interim. In July the values for GA3 (Fig. 4h) are lower than for ERA-Interim (Fig. 4b) and NCEP-CFSR (Fig. 4e), and the local track density maximum, near 90°E and 35°N, is less pronounced. An interesting feature is that in July all three datasets show a less elongated (west–east) main track path (Figs. 4b,e,h) than in April and September. This is most clearly seen in the GA3 track densities

(Figs. 4g–i). In September, GA3 again shows higher track densities over the central TP than in April.

The main track path of the TPVs is further explored in connection to the upper-level atmospheric circulation. Figure 5 shows the track densities for ERA-Interim (Figs. 5a,c,e) for January, April, and July together with the wind field at 200 hPa, the level where the core of the SWJ is located. The differences of the track path in summer compared to the other seasons appear to be caused by the strength and position of the SWJ, moving from south of the TP in winter to north of the TP in summer, passing the TP in spring and autumn (Schiemann et al. 2009). The wind speeds are highest over and south of the TP in January (Fig. 5a), while they are generally low in summer (Fig. 5e), when the jet stream is positioned north of the TP and the Tibetan anticyclone is visible in the 200-hPa wind field. Consequently, the TPVs do not travel as far eastward in summer as they do in spring and autumn. As soon as the SWJ moves back south in autumn the track density becomes more elongated, similar to winter and spring (not shown). Hence the strength and position of the jet stream appears to control the distance TPVs can travel eastward.

For January and April the wind field at 200 hPa in GA3 (Figs. 5b,d) is very similar to the wind field in ERA-Interim. However, in summer the Tibetan anticyclone appears to be stronger in GA3 and the jet is moved northward in the model compared to ERA-Interim (Fig. 5f). The summer jet bias in the GA3
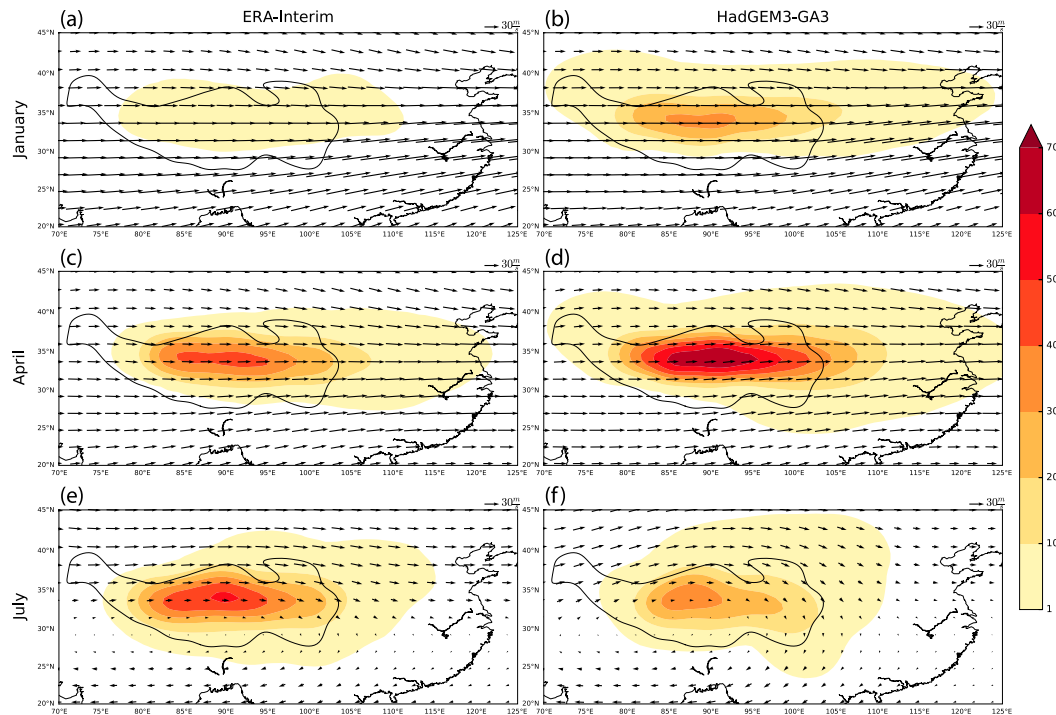
FIG. 5. Track density of all TPVs and the 200-hPa wind field for (a),(c),(e) ERA-Interim and (b),(d),(f) the HadGEM3-GA3 ensemble mean (regridded to the ERA-Interim grid) for (top) January, (middle) April, and (bottom) July. The color shading shows the track density in number per month per unit area (using a 5° spherical cap), while the black arrows show the mean 200-hPa wind field (every third grid point displayed for clarity). The boundary of the TP is indicated using the 3000-m contour.

model is consistent with the drop in the number of generated TPVs in July and August as seen in the annual cycle of TPV occurrence (section 3; Fig. 2).

The scatterplot in Fig. 6 clearly shows the strong relationship between the distance TPVs travel and the wind speed at 200 hPa (averaged over the main track density region) for ERA-Interim and GA3. This relationship is statistically significant at the 99% level with correlation coefficients of 0.803 for ERA-Interim and 0.846 for GA3, leading to high values of explained variance (R^2) of 64% and 72%, respectively. This relationship exhibits a strong annual cycle with very similar characteristics in both datasets; in winter higher wind speeds at 200 hPa are related to longer distances traveled, whereas in summer the wind speed is lower and consequently the traveled distances are shorter. The higher number of moving-off TPVs in spring and autumn, visible in all datasets (Fig. 2), also agrees with this interpretation.

(ii) Lysis

Figure 7 shows the lysis densities. Most of the TPVs die out over the TP. The highest lysis densities are found in an area around 90°–100°E all year round. Compared

to ERA-Interim (Figs. 7a–c), the local maximum in the central TP is more pronounced in NCEP-CFSR (Figs. 7d–f) in spring and autumn, whereas it is less strong in summer but covers a larger area. NCEP-CFSR also shows more TPVs dying out to the east of the TP
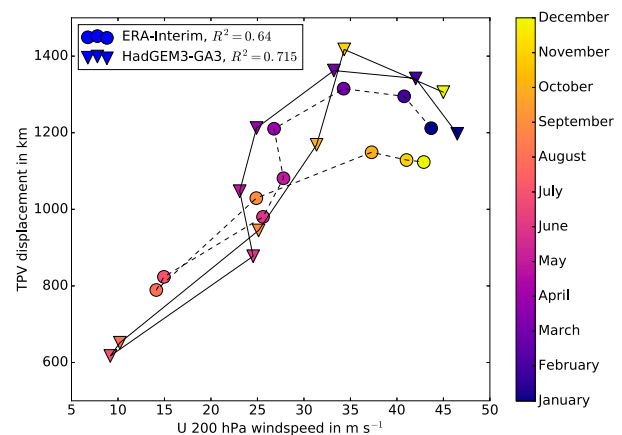

FIG. 6. Scatterplot of *u* (zonal) wind speed at 200 hPa, averaged over the main track region (33°–35°N, 85°–95°E), against TPV displacement (calculated as distance between start and end point of tracks), for ERA-Interim (dots) and the HadGEM3-GA3 ensemble mean (triangles) for each month.
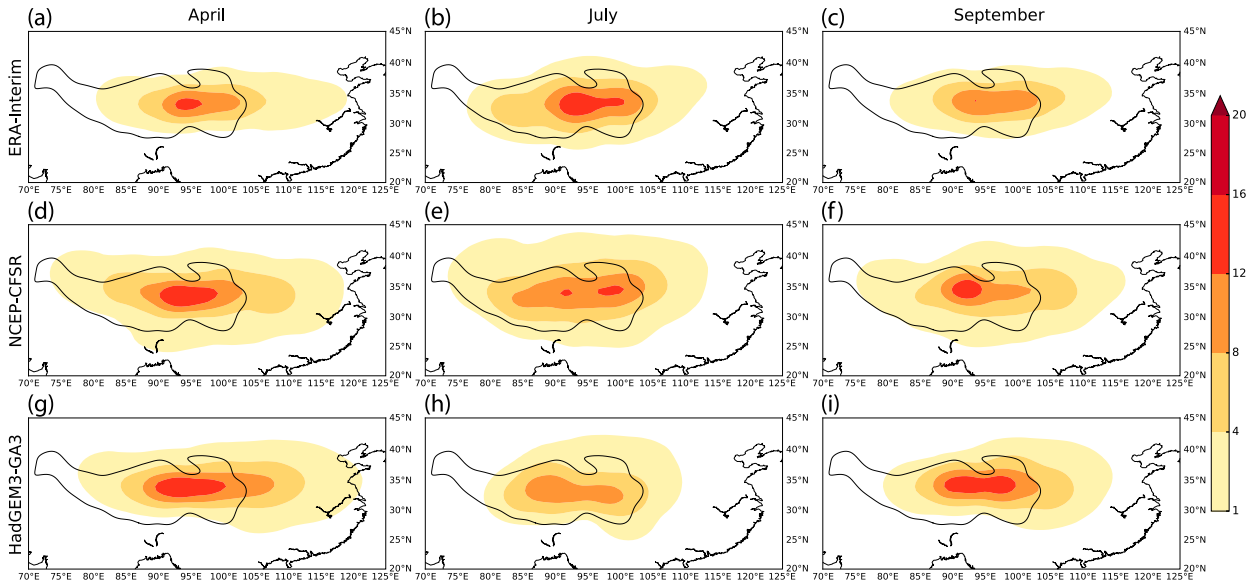
FIG. 7. Lysis density of all TPVs for (a)–(c) ERA-Interim, (d)–(f) NCEP-CFSR, and (g)–(i) the HadGEM3-GA3 ensemble mean for (left) April, (center) July, and (right) September. The color shading shows the lysis density in number per month per unit area (using a 5° spherical cap). The boundary of the TP is indicated using the 3000-m contour.

than in ERA-Interim, mainly in April and September. In general the lysis densities derived from NCEP-CFSR cover a larger area east of the TP and with a larger north–south extent than in ERA-Interim. The eastward extent of the lysis region is similar for both reanalysis datasets: TPVs can travel as far as 118°E in spring, nearly reaching the coast of the East China Sea and the Yellow Sea. One has to bear in mind that these densities are only climatological values; individual TPVs can travel farther east than 118°E. The region where TPVs die out reaches farther west in NCEP-CFSR (up to 74°E) than in ERA-Interim, where it reaches only to ~80°E in April and September and toward ~77°E in July.

GA3 (Figs. 7g–i) shows generally similar results for the lysis densities compared to the reanalysis datasets but is slightly closer to NCEP-CFSR than ERA-Interim. In July the local maximum is less pronounced or weaker in GA3 than in ERA-Interim and NCEP-CFSR, whereas it is stronger in September, confirming the results from track densities. The lower GA3 track and lysis densities in July are consistent with the fewer TPVs identified in GA3 in July compared to the two reanalysis datasets (Fig. 2). The north–south and west–east extents of the lysis region in the GA3 ensemble lie in between the extents of the two reanalysis datasets.

b. Moving-off TPVs

Since the moving-off TPVs are the ones that potentially can impact the downstream areas of China, we computed the spatial statistics for the subsample of all

TPVs that travel farther east than 105°E. Figure 8 shows a bipolar structure for the genesis densities in the reanalysis datasets for all three months, with a local maximum in the northwestern part of the TP, where the main genesis region for all TPVs is located, and a second local maximum in the eastern part of the TP, close to the eastern edge of the TP. In April, ERA-Interim exhibits the maximum genesis density at the western local maximum while NCEP-CFSR shows the highest number of generated TPVs at the eastern genesis maximum. In July (Figs. 8b,e,h) the number of moving-off TPVs is generally lower than in spring and autumn for both reanalysis datasets and therefore the densities show only weak maxima, but the bipole structure is still visible. In September the genesis density again looks similar to the April pattern but with lower maximum values.

The differences between the reanalysis data and the GA3 ensemble mean are bigger for the genesis densities of moving-off TPVs (Fig. 8) than for all TPVs (Fig. 3). In April, GA3 shows a bipolar structure similar to ERA-Interim and NCEP-CFSR but exhibits similarly high values at both local maxima, whereas there is a distinct primary maximum over the western (eastern) TP in ERA-Interim (NCEP-CFSR). In July, the genesis density pattern seen in GA3 is different from that in ERA-Interim and NCEP-CFSR, with two weak maxima in the northeastern and southeastern parts of the TP, respectively. The maximum in the western part of the TP is missing. The bipole pattern between west and east is then re-established in autumn with the primary maximum in
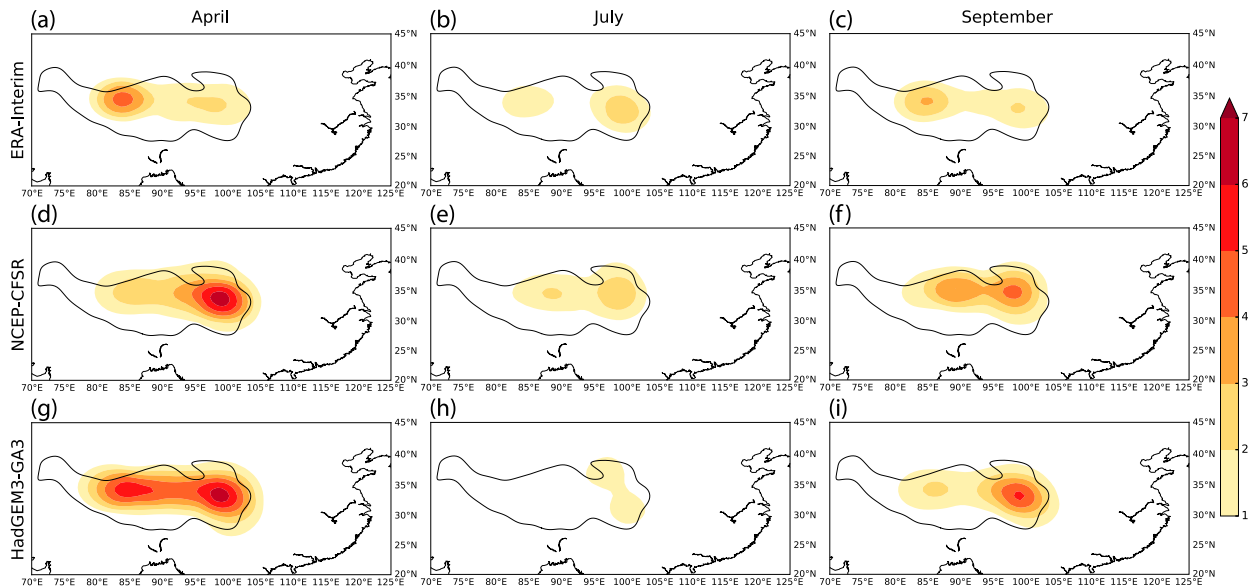
FIG. 8. Genesis density of moving-off TPVs for (a)–(c) ERA-Interim, (d)–(f) NCEP-CFSR, and (g)–(i) the HadGEM3-GA3 ensemble mean for (left) April, (center) July, and (right) September. The color shading shows the genesis density in number per month per unit area (using a 5° spherical cap). The boundary of the TP is indicated using the 3000-m contour.

the eastern part of the TP, showing higher genesis densities than ERA-Interim and similar values to NCEP-CFSR. The large differences in the density values in April and September between GA3 (Figs. 3g,i) and ERA-Interim (Figs. 3a,c) are consistent with the higher number of identified moving-off TPVs in GA3, as visible in the annual cycle (Fig. 2).

The track densities for the moving-off TPVs show generally similar results for the reanalysis data and the model (not shown). The band of high track densities for moving-off TPVs is shifted eastward compared to that for all TPVs, as is expected given the definition of moving-off TPVs.

Moving-off TPVs mainly die out between 103° and 115°–120°E (not shown), with the highest lysis densities occurring in April between 105° and 110°E and the lowest lysis densities occurring in summer. In April and September, GA3 and NCEP-CFSR are in closer agreement than the two reanalysis datasets.

c. Heavy-rain TPVs

Since TPVs are known to be able to trigger heavy precipitation and also severe flooding downstream of the TP (e.g., in the Yangtze River valley), we examine the spatial statistics of heavy-rain TPVs to see whether they are generated in the same regions and show similar paths as the majority of TPVs.

The annual cycle in section 3 shows that most of the TPVs associated with high precipitation amounts (heavy-rain TPVs) occur in the extended summer season

(April–September). Therefore we show the spatial densities only for July (Fig. 9) as the results are similar in other summer months.

ERA-Interim (Figs. 9a–c) and NCEP-CFSR (Figs. 9d–f) are in good agreement for all densities (genesis, track, lysis). The genesis densities for ERA-Interim (Fig. 9a) and NCEP-CFSR (Fig. 9b) both show a maximum in the southeastern TP extending westward to the area of the main genesis region for all TPVs.

The GA3 ensemble mean shows a more pronounced genesis density maximum (Fig. 9g) at the southeastern edge of the TP compared to the reanalysis datasets, but a similar westward extension to the central TP with slightly lower density values.

In ERA-Interim and NCEP-CFSR, the heavy-rain TPVs travel mainly eastward along the same latitude as found for the track density for all TPVs (Figs. 9b,e). GA3 again shows a different picture for the TPV paths (Fig. 9h): it seems that they are mainly stationary systems or only travel short distances northeastward or southeastward from their main genesis region.

The lysis density for GA3 (Fig. 9i) reveals nearly the same spatial pattern as the track density, while the heavy-rain TPVs in ERA-Interim and NCEP-CFSR die out either in the region close to the Brahmaputra channel at the southeastern border of the TP or directly after moving off the TP to the east. These results show that heavy-rain TPVs do not travel far away from the TP and can therefore only directly affect regions on the TP or its immediate vicinity.
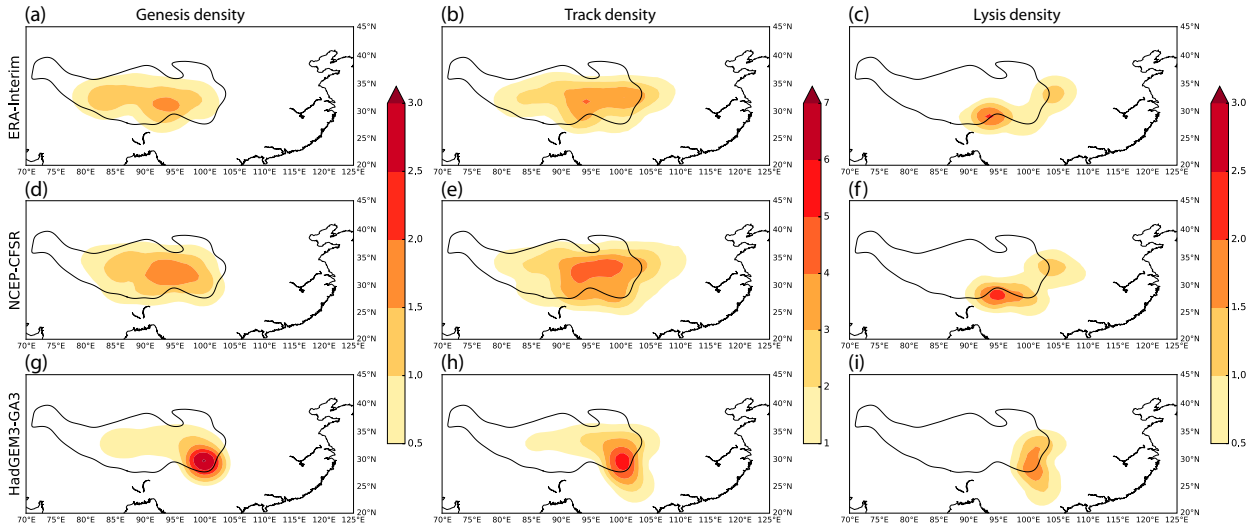
FIG. 9. (left) Genesis, (middle) track, and (right) lysis density of heavy-rain TPVs for (a)–(c) ERA-Interim, (d)–(f) NCEP-CFSR, and (g)–(i) the HadGEM3-GA3 ensemble mean for July. The color shading shows the genesis density in number per month per unit area (using a 5° spherical cap). The boundary of the TP is indicated using the 3000-m contour.

It is not surprising that GA3 shows differences regarding the position and intensity of the genesis, track, and lysis densities for heavy-rain TPVs, since the model not only has to capture the TPVs but also has to simulate the correct amount of associated precipitation. It is possible that the differences in the location of heavy-rain TPVs in GA3 compared to the reanalyses are related to a precipitation bias in GA3. Bush et al. (2015) showed [albeit in a low resolution (N96) version of GA3] a strong positive precipitation bias in the same region where most of the heavy-rain TPVs are identified.

5. Lifetime and displacement

In this section we will analyze the distributions of lifetime and the distance TPVs can travel for the three datasets and the three subsets of TPVs (all, moving-off, heavy-rain). Since the majority of TPVs occur in the extended summer season (April–September), we limit the analysis to this period.

Figure 10 shows the average distribution of TPV lifetime. The distribution of lifetimes for all TPVs shows a clear maximum at the shortest lifetimes; 17% of the TPVs have a lifetime of 24 h and around 60% of TPVs have lifetimes between 24 and 42 h. The percentage of TPVs decreases exponentially with longer lifetimes; TPVs with lifetimes over 84 h account for only 5% of the TPVs. The different datasets show similar lifetime distributions. Previous studies generally state that TPVs are mainly short-lived systems with lifetimes below 24 h, with an average lifetime varying between 15 and 18 h. Since we are only interested in and track TPVs

that are persistent for at least 24 h, a quantitative comparison with previous studies is difficult, but the general distribution with a maximum toward shorter lifetimes is captured.

The lifetime distribution for the moving-off TPVs differs from that for all TPVs. Here, the distribution is slightly shifted toward longer lifetimes compared to the average over all TPVs, leading to a broader distribution. In ERA-Interim and NCEP-CFSR the maximum of the distribution occurs at lifetimes between 36 and 42 h. From 42 h onward the distributions for both reanalyses show a decrease of TPV number with increasing lifetime. In GA3 the lifetime distribution of the moving-off TPVs has its peaks at lifetimes between 42 and 48 h.

In the GA3 ensemble mean there are relatively more long-lived heavy-rain TPVs than in the reanalyses. Only 10% of the heavy-rain TPVs in GA3 have lifetimes of 24 h compared to 15% in both reanalyses. While the lifetime distribution of heavy-rain TPVs in both reanalyses have their maximum at lifetimes between 24 and 30 h (15%), the percentage of heavy-rain TPVs with this lifetime is lower in GA3 (10%) but the distribution exhibits another maximum at lifetimes between 36 and 42 h. For lifetimes greater than 66 h the curve for the lifetime distribution of heavy-rain TPVs in GA3 is basically the same as for moving-off TPVs.

For the moving-off TPVs and especially the heavy-rain TPVs the spread between the three datasets is larger than for all TPVs, which is very likely due to the much smaller sample size for heavy-rain TPVs.

Figure 11 shows the distances TPVs travel during their lifetime, the displacement is calculated as the "crow
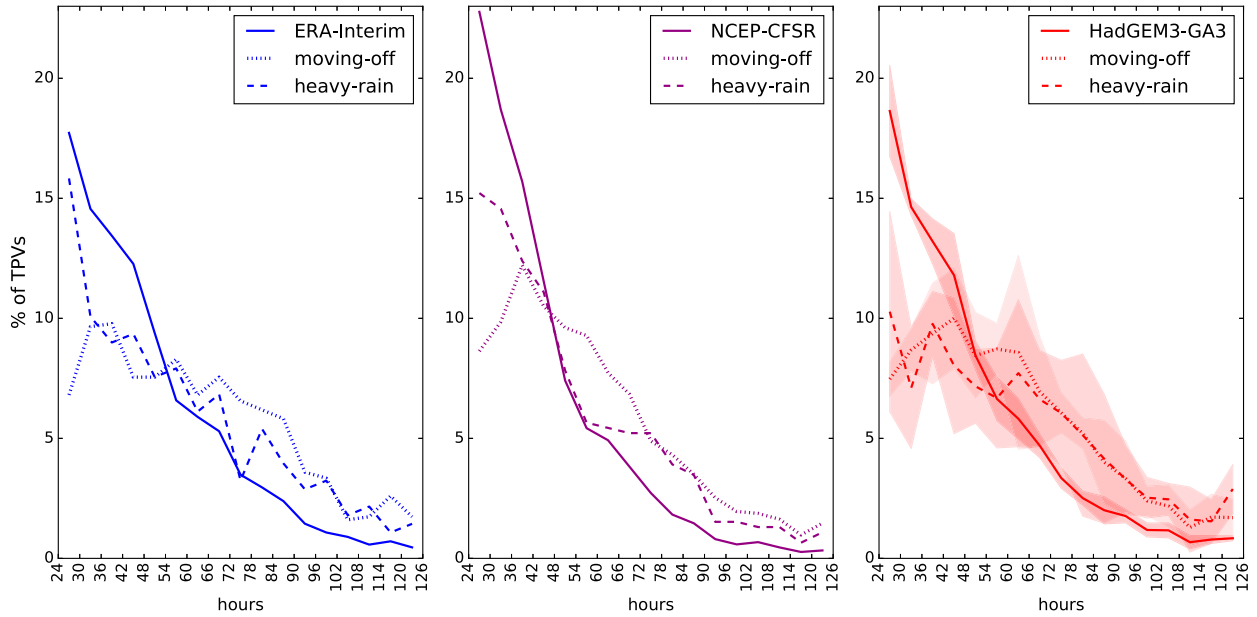
FIG. 10. Lifetime distribution for all TPVs (solid), moving-off TPVs (dotted), and heavy-rain TPVs (dashed) for ERA-Interim (blue), NCEP-CFSR (purple), and the HadGem3-GA3 ensemble mean (red; shading shows the standard deviation within the ensemble) for the extended summer season (April–September).

flies'' (shortest) distance between the start and end points of the tracks. Most of the TPVs travel between 0 and 1250 km, with a maximum at distances between 500 and 750 km for ERA-Interim and between 250 and 500 km for NCEP-CFSR and GA3. For distances larger than the modal distance, the number of TPVs decreases

rapidly with increasing distance traveled. The distribution is shifted toward longer distances when the distance traveled is accumulated over all points of the tracks (not shown). This suggests that some of the TPVs with short as-the-crow-flies distances are quasi stationary and move around in a small area on the TP. The reanalysis
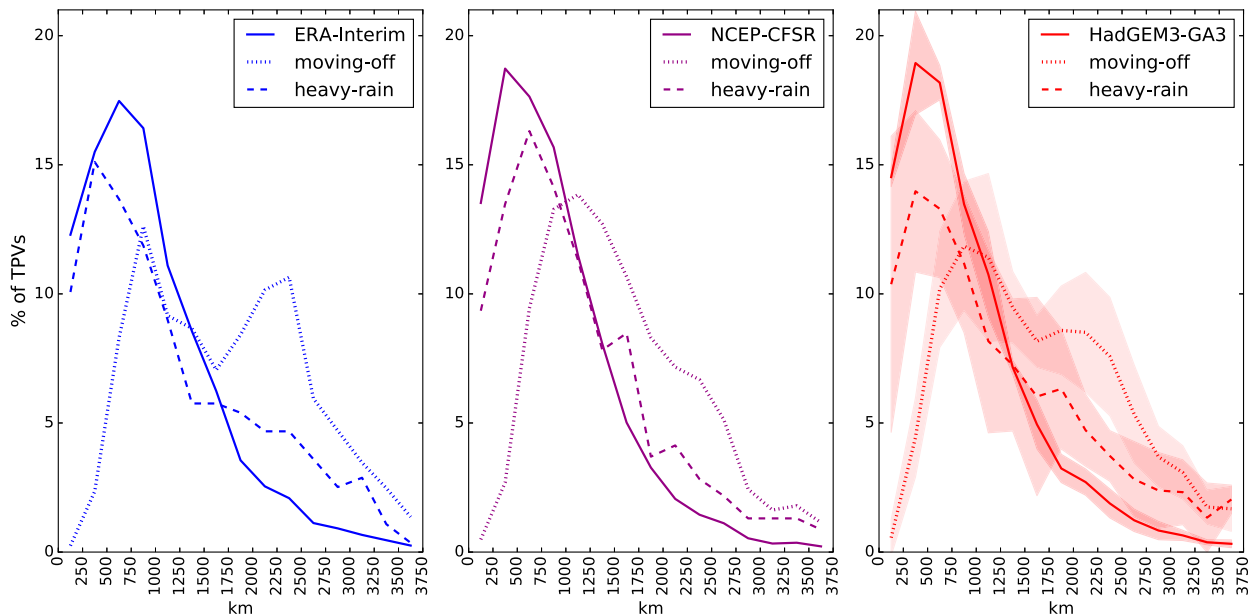

FIG. 11. Displacement (traveled distance calculated as distance between start and end point of the TPV tracks) of all TPVs (solid), moving-off TPVs (dotted), and heavy-rain TPVs (dashed) for ERA-Interim (blue), NCEP-CFSR (purple), and the HadGEM3-GA3 ensemble mean (red; shading shows the standard deviation within the ensemble) for the extended summer season (April–September).
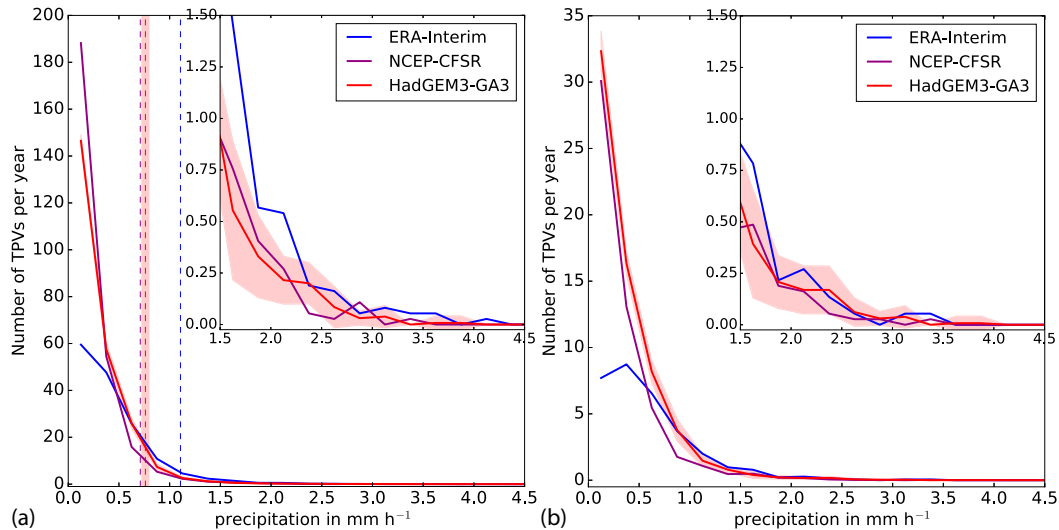
FIG. 12. Distribution of maximum-attained precipitation along TPV tracks for (a) all TPVs and (b) moving-off TPVs for ERA-Interim (blue), NCEP-CFSR (purple), and the HadGEM3-GA3 ensemble mean (red). The red shading covers the spread between the five HadGEM3-GA3 ensemble members, its upper and lower boundary is defined as $\pm 2\sigma$ from the mean over the five ensemble members. The dashed lines in (a) denote the 95th percentile thresholds; ensemble mean value plotted for HadGEM3-GA3 since the thresholds for the five ensemble members are very close together and the lines would be on top of each other.

data and model simulations show very similar results for the displacement distribution of all detected TPVs.

The moving-off TPVs generally travel larger distances. The distribution shows a rapid increase of TPV numbers from a very low percentage of TPVs traveling distances of 0–250 km (1%) toward a maximum at distances between 750–1000 (1000–1250) km for ERA-Interim and GA3 (NCEP-CFSR). The distribution shows wider maxima in NCEP-CFSR and GA3, while ERA-Interim exhibits a second maximum of similar magnitude at distances between 2250 and 2500 km. This secondary maximum is also visible in GA3 but has a lower magnitude than the primary maximum in GA3. The two maxima in ERA-Interim are about 1200 km apart, which reflects the distance between the two main genesis regions for moving-off TPVs in ERA-Interim (section 4b). One of the main genesis regions for moving-off TPVs is located in the northwestern part of the TP (Fig. 8). TPVs originating there have to travel longer distances to reach regions east of 105°E, which is the condition we have imposed for them to be classed as moving-off TPVs, than the ones originating in the eastern part of the TP. This might account for the shift toward longer distances traveled. The slightly higher variations among the datasets are caused by the smaller sample size as discussed earlier.

Heavy-rain TPVs show displacement distributions similar to one another in all three datasets, with a maximum at distances between 250 and 500 km in

ERA-Interim and GA3 and a maximum at 500–750 km in NCEP-CFSR.

For all three datasets the percentage of TPVs traveling longer distances (>1500 km) is higher for moving-off and heavy-rain TPVs compared to all TPVs.

6. Precipitation associated with TPVs

Figure 12 shows the precipitation intensity distribution for the maximum-attained precipitation along the tracks for all TPVs (Fig. 12a) and the moving-off TPVs (Fig. 12b) with a zoom-in to the tail of the distributions. The heavy-rain TPVs are included in these. The distributions show that most TPVs are associated with low amounts of precipitation for both groups of TPVs. The 95th percentile maximum precipitation thresholds (vertical dotted lines in Fig. 12a) are not located in the tail of the distributions, which emphasizes that even TPVs with relatively low hourly precipitation rates (above $1\,\mathrm{mm\,h^{-1}}$; i.e., $24\,\mathrm{mm\,day^{-1}}$) fall within the group of heavy-rain TPVs; thus, the vast majority of TPVs are associated with lower maximum precipitation rates.

To examine how much of the monthly precipitation over the Tibetan Plateau and its surroundings is associated with TPVs, we calculate the total TPV-associated precipitation and the ratio between the total precipitation and TPV-associated precipitation for ERA-Interim and the GA3 ensemble (Fig. 13; see also Figs. S1–S3 in the online supplemental material).
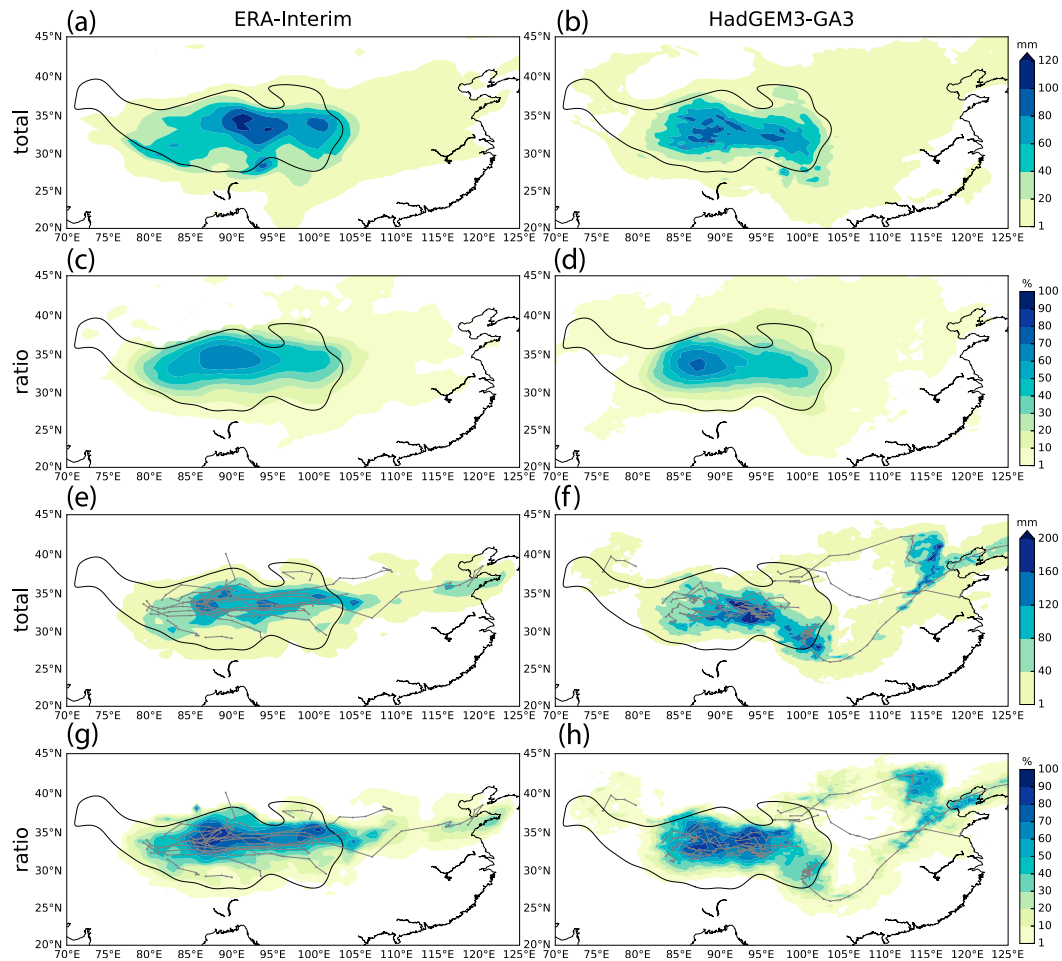
FIG. 13. (a),(b) Climatological total TPV-associated precipitation and (c),(d) climatological ratio (%) of TPV-associated precipitation to total precipitation for July for (a),(c) ERA-Interim (1980–2015) and (b),(d) the HadGEM3-GA3 ensemble mean (1986–2011). (e),(f) Total TPV-associated precipitation and (g),(h) ratio of TPV-associated precipitation to total precipitation and TPV tracks (gray lines) for (e),(g) ERA-Interim for July 2008 and (f),(h) the HadGEM3-GA3 ensemble member xgxqe for July 2006. The boundary of the TP is indicated using the 3000-m contour.

Figure 13 shows the average total of TPV-associated precipitation and the average contribution of TPV-associated precipitation to the total precipitation in July for ERA-Interim (Figs. 13a,c) and for the GA3 ensemble mean (Figs. 13b,d). Here we focus on July since this is the month where the number of TPVs is highest and extreme precipitation events affecting the regions downstream of the TP were reported (see introduction). Precipitation associated with TPVs occurs in all areas where TPVs are active. In July, the TPV-associated precipitation reaches 80–100 mm over the central TP for both datasets, with a slightly higher maximum (around 120 mm) in ERA-Interim. The ratio in Fig. 13c shows that TPVs account for 40%–70% of the total precipitation over the central TP and for 10%–40% in most other parts of the TP (except regions west of the

main genesis region, since the TPVs mainly travel eastward), confirming the statement by Wang (1987) that TPVs are one of the main precipitation-producing systems on the TP. For NCEP-CFSR the same analysis shows a similar pattern but lower values (not shown).

The area affected by precipitation associated with TPVs extends to the east into the downstream regions of the TP (Sichuan province) and to the southeast, still accounting for 10%–20% of the total precipitation. The Sichuan province is known to be affected by TPVs causing extreme precipitation and flooding. The southeastward extension of the contribution of TPVs to the total precipitation in the eastern part of the TP might be caused by higher moisture availability in this region in summer due to the high moisture transport through the Brahmaputra channel located at the southeastern border

TABLE 2. Selected years of high and low TPV frequency.

Month	High TPV count years	Low TPV count years
May	1984, 1992, 2003, 2005, 2013	1990, 1995, 2001, 1994, 2000, 2002
June	1979, 2002, 2009, 2010	1981, 1991, 1997, 2013
July	1984, 1993, 1998, 2004	1989, 1997, 2002, 2015
August	1980, 1998, 2003, 2005, 2006	1983, 1984, 1986, 1990, 2002

of the TP. The Brahmaputra channel is one of the major moisture pathways connecting the TP with the Indian subcontinent and therefore with the moisture-laden monsoon air masses (Curio et al. 2015).

The GA3 ensemble (Figs. 13b,d) shows very similar results regarding the climatological total TPV-associated precipitation and contribution of TPV-associated precipitation to the total precipitation and its spatial distribution. This result means that the model is not only able to capture TPV occurrence, but also largely captures the amount of TPV-associated precipitation and therefore the correct meteorology leading to precipitation. The southeast extension is somewhat larger in the GA3 ensemble mean than in ERA-Interim, consistent with results shown for heavy-rain TPVs (Fig. 9).

For single months (Figs. 13e–h) the total TPV-associated precipitation and the contribution of TPVs to the total monthly precipitation can be much higher. Figure 13g shows the TPV contribution to the total precipitation for ERA-Interim in July 2008, where TPVs account for up to 90% of the total monthly precipitation over the central TP, with values of more than 120 mm of total TPV-associated precipitation (Fig. 13e). This selected month also shows that TPVs can have a big impact on the total precipitation downstream of the TP, up to 40% in the Sichuan region, directly east of the TP, and up to 30% at the coast just north of 35°N. This high contribution to the total monthly precipitation was, in this case, caused by a single TPV moving all the way from the TP to the coast of the Yellow Sea (see Fig. 1). This TPV corresponds to the observed TPV described in the introduction (Feng et al. 2014).

For individual GA3 ensemble members the contribution of TPVs to the total monthly precipitation can also be higher downstream of the TP in single years. For example, in the GA3 ensemble member xgxqe in July 2006 (Fig. 13h) a single TPV accounted for up to 70% of the total monthly precipitation over eastern China, due to a total TPV-associated precipitation of more than 120 mm in some regions.

Additionally, the supplemental material shows the total TPV-associated precipitation and the contribution of TPVs to the total precipitation for all (Fig. S1), moving-off (Fig. S2), and heavy-rain (Fig. S3) TPVs for selected months (April, July, September) for ERA-Interim and the GA3 ensemble mean. Moving-off TPVs (Fig. S2) produce more precipitation in April and September at the eastern edge of the TP and directly east of the TP compared to July, which coincides with the higher number of moving-off TPVs during these months as shown in section 3. The contribution of heavy-rain TPVs to the total precipitation is low (up to 10%) for all months and regions, even in July when the average total TPV-associated precipitation reaches more than 50 mm in some parts of southwest China and the southeastern edge of the TP (Fig. S3). This confirms that the importance of TPV-associated precipitation arises from individual events and cannot be assessed by considering climatological values only.

7. Interannual variability

The analysis so far suggests that the position and strength of the SWJ has an influence on the TPV occurrence and affects how far they can travel eastward since the jet acts as the dominant steering flow. To examine whether there is also a connection between the interannual variability of TPV frequency and the SWJ position, we selected years featuring the highest and lowest TPV counts in ERA-Interim for May, June, July, and August, respectively. Table 2 shows the years considered for each month. The number of selected years varies because for some months, multiple years exhibit the same TPV count.

Using the selected years we calculate the probability that a point is in a westerly jet, and in a further step calculate the difference in this probability between years with high and low TPV frequencies, following the methodology used by Hunt et al. (2018a). To do so a point is defined as being in the SWJ, if the following conditions are met at the 200-hPa level using 6-hourly ERA-Interim data: the wind is westerly ($u > 0$) and the magnitude of its speed is greater than $30 \, \mathrm{m \, s}^{-1}$ (e.g., Schiemann et al. 2009). Since the position of the jet has a pronounced annual cycle this calculation is done for each month separately.

Figure 14 shows the difference in jet position between years with high and low TPV frequency for May, June, July, and August in ERA-Interim.

In May (Fig. 14a) the jet is more likely to be in a position south of 35°N (blue shading) for years with a high
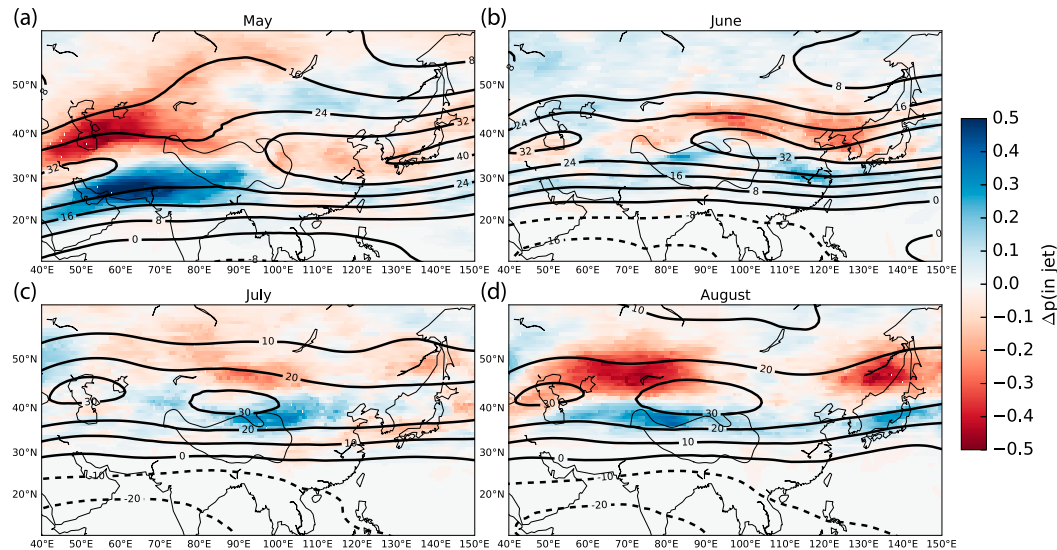
FIG. 14. Difference in westerly jet location between years of high and low TPV frequency for ERA-Interim in (a) May, (b) June, (c) July, and (d) August. The thick black contours show the climatological mean of u wind speed at 200 hPa in m s^{-1}. The boundary of the TP is indicated using the 3000-m contour.

TPV frequency, whereas in years with a low TPV frequency the jet is more likely to occur north of 35°N (red shading). This signal is strongest upstream of the TP. This could mean that the jet is stronger in this more southerly position and also probably more constrained to certain latitudes. In years with low TPV frequency the jet appears to be less zonal. In spring the jet is undergoing a transition from winter to summer positions, south to north of the TP respectively, and the springtime transition is less gradual than in autumn; this results in split jets being likely to occur (Schiemann et al. 2009). In May the signal is stronger than in June and July, when the jet is already located at the northern edge of the TP. This reflects the fact that in spring the position of the jet is more variable and the interannual variability is higher.

In summer (June, July, and August; Figs. 14b–d) more TPVs occur when the jet is positioned closer to the TP, south of its climatological mean position, which means higher wind speeds over the TP and in general a larger influence of the jet on the TP. Li et al. (2014) state that the right-hand side of the jet core provides favorable conditions for TPV generation and eastward movement due to associated low-level (500 hPa) convergence and upper-level (200 hPa) divergence.

8. Summary and conclusions

In this study we compared the climatologies of TPVs that we identified and tracked in two reanalysis datasets (ERA-Interim and NCEP-CFSR) and a high-resolution global climate model (HadGEM3-GA3), using the objective feature-tracking algorithm TRACK (Hodges 1995). We assessed how well the model represents the TPV climatology and discussed how TPV occurrence is linked to the subtropical westerly jet (SWJ) and therefore the large-scale atmospheric circulation. The main results and conclusions are summarized below:

- The HadGEM3-GA3 model is able to simulate TPVs at N512 horizontal resolution (about 25 km grid spacing).
- The reanalysis data and the model show similar results for the spatial statistics of TPVs. Most TPVs are generated in the northwestern part of the TP. The center of this main genesis region is small and stable throughout the year. TPVs move mainly eastward in a band of high track density along 34°N.
- The SWJ acts as the main steering flow for the TPVs. The strength and position of the subtropical westerly jet is correlated with the distance TPVs can travel eastward and therefore could have an effect on whether or not a TPV is moving-off the TP. The interannual variability of the jet position is correlated to the interannual variability of the number of generated TPVs, especially in months when the interannual variability of the jet location is high. Based on these statistical relationships we hypothesize a role of the SWJ in the interannual variability and the annual cycle of TPV occurrence frequency, but the dynamical connection is unclear and will be the subject of a future study.
- TPVs that move off the TP to the east are generated in two main genesis regions, the northwestern TP and the

eastern TP. For moving-off TPVs, the differences between the reanalysis data and the GA3 simulations are larger than for all TPVs. The average lifetime is slightly longer for moving-off TPVs and the traveled distance is also larger compared to the average over all TPVs.

- Precipitation associated with TPVs accounts for up to 70% of the total precipitation over the central TP in July. For individual years this ratio can reach up to 90% in some regions of the TP.
- While their climatological impact on the total precipitation over the mainland of China is low (up to 10%), TPVs can account for up to 40% (70%) of the total precipitation in selected months in ERA-Interim (GA3). Therefore TPVs have a high impact on the mainland of China due to individual events, which makes it important to understand the conditions under which these events can occur.

We have presented what is, to our knowledge, the first TPV climatology from a global climate model. The fact that our global climate model can represent the TPV climatology opens a wide range of options for future model-based research on TPVs.

Future work will include analyses of the variability of TPV activity and its remote and local drivers, e.g., the examination of possible connections with large-scale features such as the Madden–Julian oscillation, ENSO, and a more detailed analysis of the connection to the subtropical westerly jet stream. Establishing a robust relationship with any of these features would suggest some degree of predictability in TPV numbers in a given season. An analysis of the connection between the interannual variability of TPVs and western disturbances (a type of storm system that propagates on the jet and tends to occur farther south, yielding heavy precipitation in the Hindu Kush/Himalaya region of northern India and Pakistan) by Hunt et al. (2018b) showed that the occurrence frequencies of both systems are strongly influenced by the location and interannual variability of the SWJ.

Composite analyses could be used, in combination with other variables (wind, moisture), to examine the vertical and horizontal structure of TPVs and the differences between different synoptic conditions. This could help to understand under which conditions TPVs are able to trigger extreme precipitation.

A ground validation of the TPVs identified in ERA-Interim using the observations from the Yearbook of TPVs published by the Institute of Plateau Meteorology in Chengdu (Sichuan Province) showed that using the observations TPVs are only detected after reaching the eastern TP, due to the absence of observations (sounding stations) in the western TP (Curio et al. 2018). The application of an automated tracking approach in a numerical weather prediction context could increase the lead time for real-time TPV detection, similar to that done for tropical and extratropical cyclones (Hodges and Emerton 2015; Froude 2010).

REFERENCES

Bengtsson, L., K. I. Hodges, and M. Esch, 2007: Tropical cyclones in a T159 resolution global climate model: Comparison with observations and re-analyses. *Tellus*, **59A**, 396–416, https://doi.org/10.1111/j.1600-0870.2007.00236.x.

Bookhagen, B., and D. W. Burbank, 2010: Toward a complete Himalayan hydrological budget: Spatiotemporal distribution of snowmelt and rainfall and their impact on river discharge. *J. Geophys. Res.*, **115**, F03019, https://doi.org/10.1029/2009JF001426.

Bush, S. J., A. G. Turner, S. J. Woolnough, G. M. Martin, and N. P. Klingaman, 2015: The effect of increased convective entrainment on Asian monsoon biases in the MetUM general circulation model. *Quart. J. Roy. Meteor. Soc.*, **141**, 311–326, https://doi.org/10.1002/qj.2371.

Curio, J., F. Maussion, and D. Scherer, 2015: A 12-year high-resolution climatology of atmospheric water transport over the Tibetan Plateau. *Earth Syst. Dyn.*, **6**, 109–124, https://doi.org/10.5194/esd-6-109-2015.

——, Y. Chen, R. Schiemann, A. G. Turner, K. C. Wong, K. I. Hodges, and Y. Li, 2018: Comparison of a manual and an automated tracking method for Tibetan Plateau vortices. *Adv. Atmos. Sci.*, **35**, 965–980, https://doi.org/10.1007/s00376-018-7278-4.

Dee, D. P., and Coauthors, 2011: The ERA-Interim reanalysis: Configuration and performance of the data assimilation system. *Quart. J. Roy. Meteor. Soc.*, **137**, 553–597, https://doi.org/10.1002/qj.828.

Dell'Osso, L., and S.-J. Chen, 1986: Numerical experiments on the genesis of vortices over the Qinghai-Tibet plateau. *Tellus*, **38A**, 236–250, https://doi.org/10.1111/j.1600-0870.1986.tb00468.x.

Dimri, A. P., D. Niyogi, A. P. Barros, J. Ridley, U. C. Mohanty, T. Yasunari, and D. R. Sikka, 2015: Western disturbances: A review. *Rev. Geophys.*, **53**, 225–246, https://doi.org/10.1002/2014RG000460.

Donlon, C. J., M. Martin, J. Stark, J. Roberts-Jones, E. Fiedler, and W. Wimmer, 2012: The Operational Sea Surface Temperature and Sea Ice Analysis (OSTIA) system. *Remote Sens. Environ.*, **116**, 140–158, https://doi.org/10.1016/j.rse.2010.10.017.

Feng, X., C. Liu, R. Rasmussen, and G. Fan, 2014: A 10-yr climatology of Tibetan Plateau vortices with NCEP Climate Forecast System Reanalysis. *J. Appl. Meteor. Climatol.*, **53**, 34–46, https://doi.org/10.1175/JAMC-D-13-014.1.

Froude, L. S. R., 2010: The predictability of extratropical cyclones (in the North Atlantic/European regions). *ECMWF Seminar on Predictability in the European and Atlantic regions*, https://www.ecmwf.int/node/15146.

Hodges, K. I., 1994: A general method for tracking analysis and its application to meteorological data. *Mon. Wea. Rev.*, **122**, 2573–2586, https://doi.org/10.1175/1520-0493(1994)122<2573:AGMFTA>2.0.CO;2.

——, 1995: Feature tracking on the unit sphere. *Mon. Wea. Rev.*, **123**, 3458–3465, https://doi.org/10.1175/1520-0493(1995)123<3458:FTOTUS>2.0.CO;2.

——, 1996: Spherical nonparametric estimators applied to the UGAMP model integration for AMIP. *Mon. Wea. Rev.*, **124**, 2914–2932, https://doi.org/10.1175/1520-0493(1996)124<2914:SNEATT>2.0.CO;2.

——, 1999: Adaptive constraints for feature tracking. *Mon. Wea. Rev.*, **127**, 1362–1373, https://doi.org/10.1175/1520-0493(1999)127<1362:ACFFT>2.0.CO;2.

——, and R. Emerton, 2015: The prediction of Northern Hemisphere tropical cyclone extended life cycles by the ECMWF ensemble and deterministic prediction systems. Part I: Tropical cyclone stage. *Mon. Wea. Rev.*, **143**, 5091–5114, https://doi.org/10.1175/MWR-D-13-00385.1.

——, R. W. Lee, and L. Bengtsson, 2011: A comparison of extratropical cyclones in recent reanalyses ERA-Interim, NASA MERRA, NCEP CFSR, and JRA-25. *J. Climate*, **24**, 4888–4906, https://doi.org/10.1175/2011JCLI4097.1.

Hoskins, B. J., and K. I. Hodges, 2002: New perspectives on the Northern Hemisphere winter storm tracks. *J. Atmos. Sci.*, **59**, 1041–1061, https://doi.org/10.1175/1520-0469(2002)059<1041:NPOTNH>2.0.CO;2.

Huang, D.-Q., J. Zhu, Y.-C. Zhang, Y. Huang, and X.-Y. Kuang, 2016: Assessment of summer monsoon precipitation derived from five reanalysis datasets over East Asia. *Quart. J. Roy. Meteor. Soc.*, **142**, 108–119, https://doi.org/10.1002/qj.2634.

Hunt, K. M. R., A. G. Turner, and L. C. Shaffrey, 2018a: The evolution, seasonality, and impacts of western disturbances. *Quart. J. Roy. Meteor. Soc.*, **144**, 278–290, https://doi.org/10.1002/qj.3200.

——, ——, J. Curio, A. G. Turner, and R. Schiemann, 2018b: Subtropical westerly jet influence on occurrence of western disturbances and Tibetan Plateau vortices. *Geophys. Res. Lett.*, **45**, 8629–8636, https://doi.org/10.1029/2018GL077734.

Li, L., R. Zhang, M. Wen, and L. Liu, 2014: Effect of the atmospheric heat source on the development and eastward movement of the Tibetan Plateau vortices. *Tellus*, **66A**, 24451, https://doi.org/10.3402/tellusa.v66.24451.

Lin, R., T. Zhou, and Y. Qian, 2014: Evaluation of global monsoon precipitation changes based on five reanalysis datasets. *J. Climate*, **27**, 1271–1289, https://doi.org/10.1175/JCLI-D-13-00215.1.

Lin, Z., 2015: Analysis of Tibetan Plateau vortex activities using ERA-Interim data for the period 1979–2013. *J. Meteor. Res*, **29**, 720–734, https://doi.org/10.1007/s13351-015-4273-x.

Maussion, F., D. Scherer, T. Mölg, E. Collier, J. Curio, and R. Finkelnburg, 2014: Precipitation seasonality and variability over the Tibetan Plateau as resolved by the High Asia Reanalysis. *J. Climate*, **27**, 1910–1927, https://doi.org/10.1175/JCLI-D-13-00282.1.

Mizielinski, M. S., and Coauthors, 2014: High-resolution global climate modelling: The UPSCALE project, a large-simulation campaign. *Geosci. Model Dev.*, **7**, 1629–1640, https://doi.org/10.5194/gmd-7-1629-2014.

Saha, S., and Coauthors, 2010: The NCEP Climate Forecast System Reanalysis. *Bull. Amer. Meteor. Soc.*, **91**, 1015–1058, https://doi.org/10.1175/2010BAMS3001.1.

——, and Coauthors, 2014: The NCEP Climate Forecast System version 2. *J. Climate*, **27**, 2185–2208, https://doi.org/10.1175/JCLI-D-12-00823.1.

Sardeshmukh, P. D., and B. I. Hoskins, 1984: Spatial smoothing on the sphere. *Mon. Wea. Rev.*, **112**, 2524–2529, https://doi.org/10.1175/1520-0493(1984)112<2524:SSOTS>2.0.CO;2.

Schiemann, R., D. Lüthi, and C. Schär, 2009: Seasonality and interannual variability of the westerly jet in the Tibetan Plateau region. *J. Climate*, **22**, 2940–2957, https://doi.org/10.1175/2008JCLI2625.1.

Tao, S.-Y., and Y.-H. Ding, 1981: Observational evidence of the influence of the Qinghai-Xizang (Tibet) Plateau on the occurrence of heavy rain and severe convective storms in China. *Bull. Amer. Meteor. Soc.*, **62**, 23–30, https://doi.org/10.1175/1520-0477(1981)062<0023:OEOTIO>2.0.CO;2.

Tous, M., G. Zappa, R. Romero, L. Shaffrey, and P. L. Vidale, 2016: Projected changes in medicanes in the HadGEM3 N512 high-resolution global climate model. *Climate Dyn.*, **47**, 1913–1924, https://doi.org/10.1007/s00382-015-2941-2.

Walters, D. N., and Coauthors, 2011: The Met Office Unified Model Global Atmosphere 3.0/3.1 and JULES Global Land 3.0/3.1 configurations. *Geosci. Model Dev.*, **4**, 919–941, https://doi.org/10.5194/gmd-4-919-2011.

Wang, B., 1987: The development mechanism for Tibetan Plateau warm vortices. *J. Atmos. Sci.*, **44**, 2978–2994, https://doi.org/10.1175/1520-0469(1987)044<2978:TDMFTP>2.0.CO;2.

Xu, X., C. Lu, X. Shi, and S. Gao, 2008: World water tower: An atmospheric perspective. *Geophys. Res. Lett.*, **35**, L20815, https://doi.org/10.1029/2008GL035867.

Zappa, G., L. C. Shaffrey, and K. I. Hodges, 2013: The ability of CMIP5 models to simulate North Atlantic extratropical cyclones. *J. Climate*, **26**, 5379–5396, https://doi.org/10.1175/JCLI-D-12-00501.1.

——, ——, and ——, 2014: Can polar lows be objectively identified and tracked in the ECMWF operational analysis and the ERA-Interim reanalysis? *Mon. Wea. Rev.*, **142**, 2596–2608, https://doi.org/10.1175/MWR-D-14-00064.1.

Zhao, Y., 2015: A study on the heavy-rain-producing mesoscale convective system associated with diurnal variation of radiation and topography in the eastern slope of the western Sichuan plateau. *Meteor. Atmos. Phys.*, **127**, 123–146, https://doi.org/10.1007/s00703-014-0356-y.

Zhu, G., S. Chen, and C. Shoujun, 2003: A numerical case study on a mesoscale convective system over the Qinghai-Xizang (Tibet) Plateau. *Adv. Atmos. Sci.*, **20**, 385–397, https://doi.org/10.1007/BF02690797.